

Journal of  
**Applied Remote Sensing**



[RemoteSensing.SPIEDigitalLibrary.org](http://RemoteSensing.SPIEDigitalLibrary.org)

## **Design and prototype of radar sensor with Vivaldi linear array for through-wall radar imaging: an experimental study**

Betül Yılmaz  
Caner Özdemir

**SPIE.**

Betül Yılmaz, Caner Özdemir, “Design and prototype of radar sensor with Vivaldi linear array for through-wall radar imaging: an experimental study,” *J. Appl. Remote Sens.* **10**(4), 046012 (2016), doi: 10.1117/1.JRS.10.046012.

# Design and prototype of radar sensor with Vivaldi linear array for through-wall radar imaging: an experimental study

Betül Yılmaz and Caner Özdemir\*

Mersin University, Department of Electrical and Electronics Engineering, Ciftlikkoy,  
Mersin 33343, Turkey

**Abstract.** We present a radar sensor that was designed to detect and image moving objects/targets on the other side of a wall. The radar sensor was composed of a linear array of Vivaldi antenna elements, an radio frequency (RF) switch, a microcontroller unit, and an RF transceiver. For the linear array, a total of eight antenna elements were used as sensors in synthetic aperture radar (SAR) configuration in the cross-range axis to improve the resolution in this dimension. Design steps of Vivaldi antenna elements and the entire linear array were presented. After the design, the prototyping procedure and the details of the radar sensor were given. Through-the-wall radar (TWR) imaging experiments were performed for stationary and moving targets using the assembled sensor. The resultant TWR images after these experiments were presented. During the image formation, a back-projection type image focusing algorithm was implemented and applied to increase the signal-to-noise ratio of the raw images. The constructed radar images demonstrated that our radar sensor could successfully detect and image both stationary and moving targets on the other side of the wall. © 2016 Society of Photo-Optical Instrumentation Engineers (SPIE) [DOI: [10.1117/1.JRS.10.046012](https://doi.org/10.1117/1.JRS.10.046012)]

**Keywords:** through wall radar; Vivaldi antenna; remote sensing; radar imaging; array antennas and radar sensor.

Paper 16237 received Mar. 28, 2016; accepted for publication Oct. 27, 2016; published online Nov. 18, 2016.

## 1 Introduction

Through-the-wall radar (TWR) has been found to be an emerging technology for detecting and imaging objects or human activities behind walls or opaque mediums.<sup>1–3</sup> TWR has a variety of applications ranging from imaging terrorists' movements inside a building to detecting life signs in dangerous conditions such as fires and earthquakes.<sup>1–5</sup> Although TWR has become a regular technology for such applications, there are still some challenging problems to overcome. The attenuation and diffraction of electromagnetic (EM) waves while passing through the wall are important phenomena that certainly lead to difficulties for the operation of TWR. The material and the thickness of the wall are unknown for the radar operator, which also affects the success of detection and/or imaging. Furthermore, a transmitted EM wave has to pass the wall twice to reach the radar receiver which further reduces the energy of the received signal. Another important problem in TWR is the lack of resolution in the cross-range direction due to the limited number of receivers along this direction. While good resolution values can be achieved in range by using a sufficiently wide frequency band for the transmitted signal, a sharp cross-range resolution is usually hard to realize since it mainly depends on the spatial sampling of the radar sensor along this direction. Yang et al. used a phased array configuration to improve the radiation pattern characteristics of the TWR antenna.<sup>6</sup> In a different design, Ren et al.<sup>7</sup> has used a variable configuration that can be used as a phased array and also in a multiple-input multiple-output (MIMO) set-up for the UHF band of frequencies. In Ref. 8, an efficient design

---

\*Address all correspondence to: Caner Özdemir, E-mail: [cozdemir@mersin.edu.tr](mailto:cozdemir@mersin.edu.tr)

for an ultrawideband (UWB) antenna that can be used for TWR applications has been presented. Although all these designs provide improvements in antenna element design, array synthesis, and TWR system design, they do not offer improvements in the cross-range dimension by the help of a synthetic aperture radar (SAR) processing scheme.

In this work, we set out to develop a TWR sensor to increase the resolution in the cross-range axis by constructing a linear array in this dimension. Coherent processing of the collected data set would increase the signal-to-noise (SNR) ratio of the received signal, which would positively increase the probability of detection for a reliable imaging of the target.<sup>9</sup> A similar radar has been developed by Mori et al.<sup>10</sup> who have applied a frequency domain system with a linear array configuration as in the case of our work. In their study, however, they have used a multistatic configuration of the manufactured linear array in contrast to our work in which we are applying the monostatic set-up that is much simpler and more practical. Also, their application was specially tailored for Japanese wooden houses with walls made up with gypsum board such that a much higher frequency range from 10 to 20 GHz was chosen. They do not aim to operate their sensor for imaging targets on the other side of the wall. In this work, we aim to image static or moving targets behind regular walls of brick or concrete such that we have considered frequency ranges from 4 to 8 GHz. Also, our system design and control logic are somewhat different from theirs in the sense that we are using a microcontroller to control the radio frequency (RF) switch while they are using an encoder triggered control mechanism.

The organization of this paper is as follows: in Sec. 2, we briefly describe our TWR sensor starting from design steps to manufacturing processes. In the next section, we present experiments that were conducted by using the prototyped sensor. We also present the constructed TWR images after applying our back-projection type imaging algorithm<sup>10–13</sup> to the measured data collected from stationary and moving target experiments behind the wall. Measured TWR images for both experiments exhibit the effectiveness and the success of our TWR sensor and our focusing algorithm. Finally, the last section briefly summarizes our work and discusses some issues regarding the developed TWR prototype.

## 2 Through-the-Wall Radar Sensor with Eight-Element Linear Array

Commercial TWR products usually have two or four antenna receivers that unfortunately lack of resolution in the cross-range axis.<sup>14,15</sup> There is a need for improved resolution in this direction possibly by increasing the number of receivers which provides a larger antenna aperture in the cross-range axis. Therefore, the main idea is to have enough receiving sensors in the cross-range direction to have a longer synthetic aperture length, which is aimed to improve the resolution in this direction so that better resolved images can be formed in the constructed TWR images. Of course, the use of SAR processing needs to be employed to be able to focus the target scattering in the cross-range dimension. As we shall explain in detail in Sec. 3, a back-projection type SAR focusing routine will be employed for this goal. For practical usage, on the other hand, the TWR device should be easily carried which limits the number of antennas inside the array configuration. Otherwise, this situation would cause problems to the operator in terms of weight and size. By considering the antenna element type (i.e., Vivaldi antenna) and the size of the array, an array with a total of eight elements has been considered to provide reasonable resolution performance in the cross-range direction.

The block diagram of our TWR sensor is as depicted in Fig. 1. The sensor has a transceiver that is responsible for generating, sending, and receiving the RF signal, an RF switch (A-Info SP8T)<sup>16</sup> that was connected to eight-element array of Vivaldi antennas. The synchronization and the control of both the transceiver and the RF switch were achieved by a microcontroller card (Arduino Mega2560)<sup>17</sup> with the help of a laptop computer. For the structure of the array, monostatic configuration is considered because of the following reason: if quasimonostatic or bistatic configuration had been selected, then we would need twice the number of antenna elements to maintain the same range resolution, which would make the sensor very heavy and cumbersome. Second, we have considered the frequency domain stepped frequency continuous wave (SFCW) signal, i.e., vector network analyzer (VNA) waveform, to be able to maximize the dynamic range and the power sensitivity. For the frequency band between 4 and 8 GHz, in fact, our VNA can

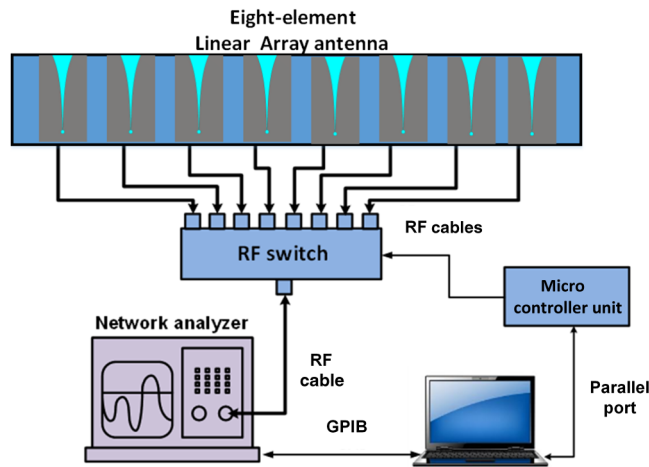


**Fig. 1** Block diagram for TWR sensor.

provide dynamic ranges of up to 92 dB, which is usually impossible to realize using a time domain system with an impulse or FMCW waveform. Furthermore, time domain pulse systems could not provide the pulse shapes for an ideal impulse shape that can be easily obtained by taking the inverse Fourier transform of the SFCW data. The imperfectness of time-pulses unfortunately negatively affects the quality of the TWR images. For this work, Agilent ENA5071B Vector Network Analyzer was used as the RF transceiver. As our MATLAB<sup>18</sup> script controls the VNA and the RF switch such that only one output port of the RF switch stays open during one-period of every  $S_{11}$  measurement, every eight consecutive  $S_{11}$  measurements provide the spatial diversity back-scattered measured data in the cross-range dimension to be used to construct one snapshot of the scene. As the  $S_{11}$  measurements continue in a time series manner, data that are responsible for multisnapshots of the scene are being collected.

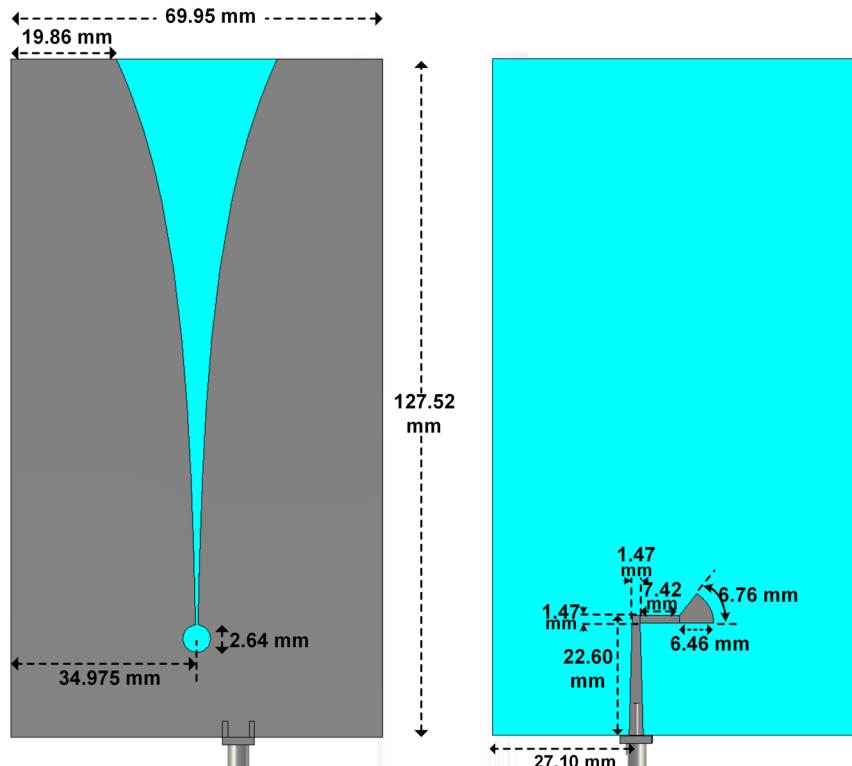


**Fig. 2** Designed Vivaldi antenna element: (a) front side and (b) back side.

The manufacturing of our TWR sensor was completed by the following steps: first, the choice of antenna elements was very crucial in order to have a successful operation. Planar antennas<sup>19,20</sup> could be good candidates for our design to be used in array configuration so that the total size and the weight of the sensor would stay within a reasonable range. We have selected the tapered slot antenna (a.k.a., Vivaldi antenna)<sup>21,22</sup> because of several reasons: (i) it has the ability of providing a UWB operation that is essential to have a sharp resolution in the range direction; (ii) It can also offer enough half-power beam width (HPBW) in the ranges between 45 and 60 deg to be able to cover the region behind the wall; and (iii) Vivaldi antennas are usually very light-weight when compared to other candidates such as horns.

We have utilized the CST Studio Suite Electromagnetic Simulator Code<sup>®23</sup> to design a Vivaldi antenna that can operate between 4 and 8 GHz with an HPBW of around 60 deg in the cross-range direction. The time domain solver option of CST has been utilized. The front and back sides of the designed antenna elements are shown in Figs. 2(a) and 2(b), respectively.

The simulation of this antenna has provided the back-scattered reflection coefficient ( $S_{11}$ ) values drawn in red, dashed line as depicted in Fig. 3, where a -10 dB frequency bandwidth of

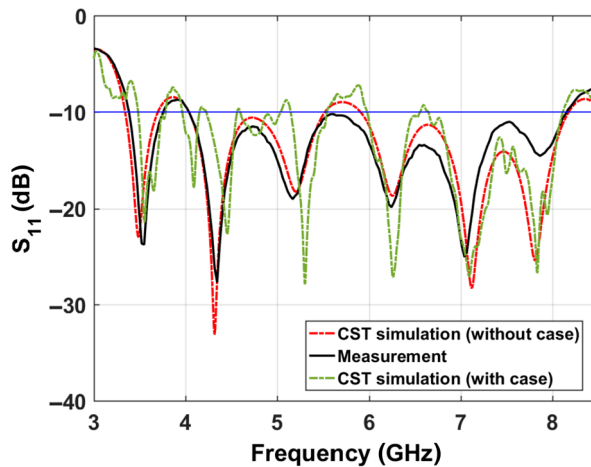


**Fig. 3**  $S_{11}$  parameter of the designed single Vivaldi antenna element [red, dashed] and measured  $S_{11}$  parameter of the produced single Vivaldi antenna element [black, solid]. Simulated  $S_{11}$  parameter of the fourth element of the radar sensor with aluminum case [red, dashed].

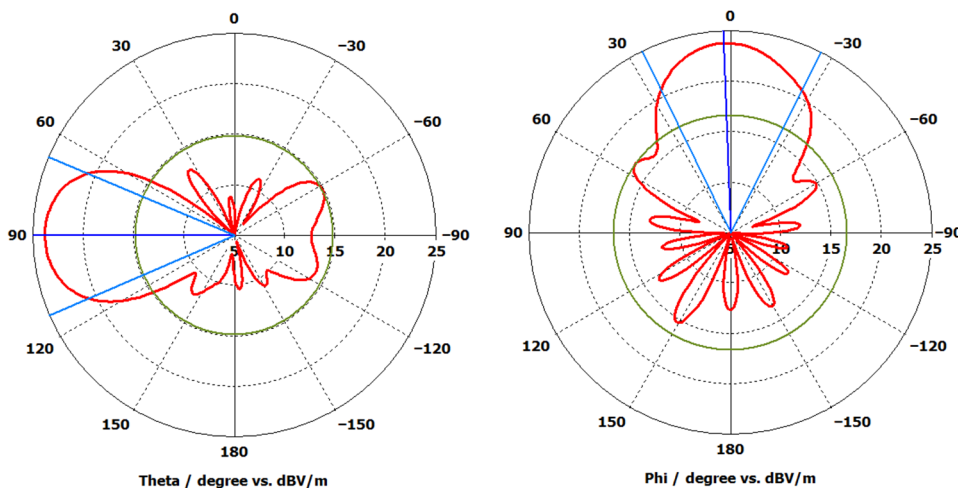


**Fig. 4** Radiation patterns for the designed Vivaldi antenna: (a)  $E$ -plane radiation pattern at  $\phi = 0$  deg and (b)  $H$ -plane radiation pattern at  $\theta = 90$  deg.

between 4 and 8 GHz is apparent. The *E*-plane and *H*-plane radiation patterns of the designed antenna for the center frequency of 6 GHz are plotted in Figs. 4(a) and 4(b), respectively. As is easily seen from Fig. 4(a), this antenna provides an HPBW of 46.1 deg along the *E*-plane direction and a maximum side lobe level (SLL) of around -8.9 dB that are acceptable values for our TWR experiments. The gain of the designed antenna element is 9.32 dB, which is fair enough for a wide radiation beam width of 46.1 deg. In Fig. 4(b), *H*-plane radiation pattern is shown.

Because 0 deg is the bearing direction of the antenna, the designed antenna has the capability of illuminating the region between -26.2 to 26.2 deg that is well suited for the operation of TWR imaging. The maximum side-lobe level is -7.1 dB and the back-lobe level is -12 dB. To further reduce the back-lobe radiation level and increase the gain of the antenna elements, designed antenna elements were put in an eight-element linear array configuration and encased by a metal box that was made of aluminum material as illustrated in Fig. 5(a). The element spacing and the size of the box were optimized by the help of CST software to minimize the mutual coupling between the antenna elements. The goal for the S-parameter optimization was  $S_{ij} < -20$  dB, ( $i \neq j$ ) for the entire frequency band between 4 and 8 GHz. After CST optimization, the minimum spacing between antenna elements was 11 cm and the corresponding TWR size becomes 88 cm together with the aluminum box case. The resultant *E*-plane and *H*-plane antenna radiation patterns for the fourth antenna from the left were obtained as illustrated in Figs. 5(b) and 5(c), respectively. During simulation of the radiation pattern of the fourth antenna, all other ports were terminated to the line impedance of  $50 \Omega$ . Thanks to the aluminum enclosure of the antenna, the gain of each element has increased to be around 11.4 dB at the mid-band frequency of 6 GHz. The reflection coefficient of the antenna element in the linear array configuration is plotted in Fig. 3 as the green, dashed line. This result is for the middle element (fourth from the left) of the eight-element Vivaldi array with the enclosing aluminum box. As can be deducted from this figure, the  $S_{11}$  characteristics do not change alter much and the bandwidth between 3.5 to 8 GHz has remained valid for almost the entire bandwidth except for the frequencies from 5.5 to 6 GHz, where the  $S_{11}$  parameter rises to be a little bit higher than -10 dB. The radiation patterns of the other antenna elements are very alike that of fourth element

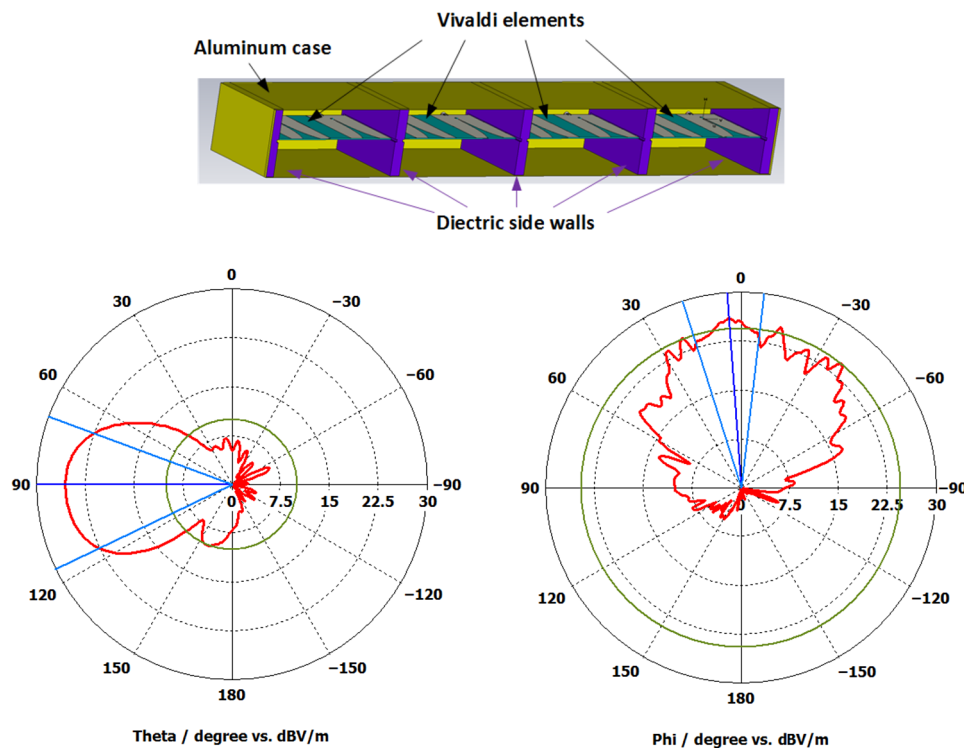


**Fig. 5** (a) Eight-element Vivaldi array inside a metal box, (b) *E*-plane radiation pattern at  $\Theta = 0$  deg, and (c) *H*-plane radiation pattern at  $\Theta = 90$  deg for the fourth element from the left.



**Fig. 6** Manufactured Vivaldi antenna element: (a) front side and (b) back side.

and do not have major shape differences. It is also worthwhile to note that the radiation pattern characteristics do not change much at the lower frequencies, whereas some distortions become apparent at the higher frequency values as sidelobe levels tend to increase. Considering that the wall penetration is much less at higher frequencies when compared to that of lower frequencies, the alteration in the radiation pattern characteristics of the antennas at higher frequencies do not have a major influence on the performance of our sensor for the TWR usage.

Once the eight-element Vivaldi array with the enclosing aluminum box was designed, the manufacturing process of the elements and the radar sensor was begun. First, each antenna element was produced with the help of an LPKF ProtoMat E33.<sup>24</sup> Pictures of the front and the back sides of the produced antenna element are shown in Figs. 6(a) and 6(b), respectively. The feeding of the antenna was realized by an subminiature version A (SMA) connector as used in the simulation. The back-scattering coefficients ( $S_{11}$ ) of the manufactured antenna elements were measured and drawn as black, solid lines in Fig. 3 with the help of the VNA. As is obvious from this figure, the measured  $S_{11}$  has been matched fairly well with the simulated one. Therefore, it was confirmed that the required bandwidth from 4 to 8 GHz was achieved for each realized Vivaldi element. Afterward, all the antenna elements were put aside with dielectric side walls that were used as separators. The case of the radar sensor was constructed aluminum metal plates with a thickness of 2 mm. The picture of the prototyped sensor is shown in Fig. 7. All antenna elements were connected to the eight terminals of the RF switch (A-Info SP8T)<sup>16</sup> with the help of semi-rigid RF cables<sup>25</sup> via SMA connectors. The control and the synchronization of VNA and the RF switch were achieved by an Arduino Mega microcontroller card<sup>17</sup> with the help of a laptop PC. A MATLAB script had been to be developed to control and command the VNA and the RF switch with the microcontroller card.

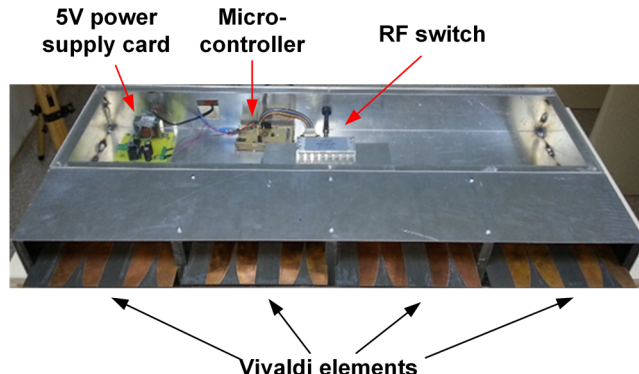


**Fig. 7** Picture of the prototyped TWR sensor.

### 3 Experimental Results

After completing the prototype of our TWR sensor, we have conducted two experiments to assess its effectiveness and the performance. For this purpose, an experiment for stationary targets and another experiment for a moving target behind the wall were done.

#### 3.1 Experiment for Stationary Targets

In this experiment, a total of three metal pipes of different sizes were put behind the wall as demonstrated in Fig. 8. The geometry of the experimental set-up is given in Fig. 8(a),

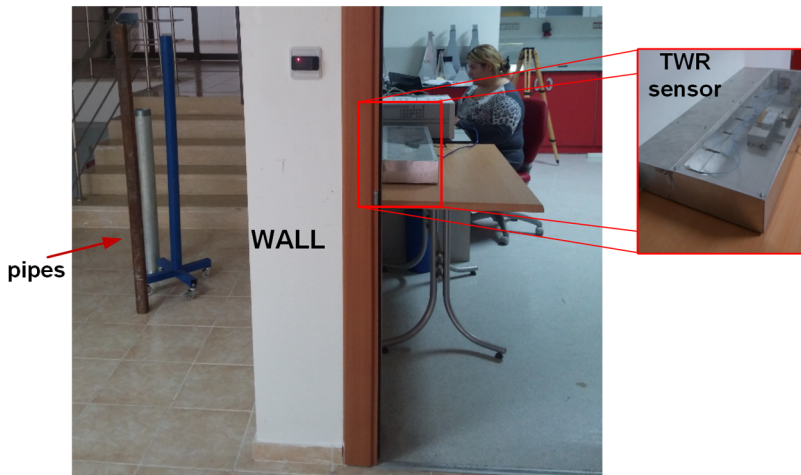
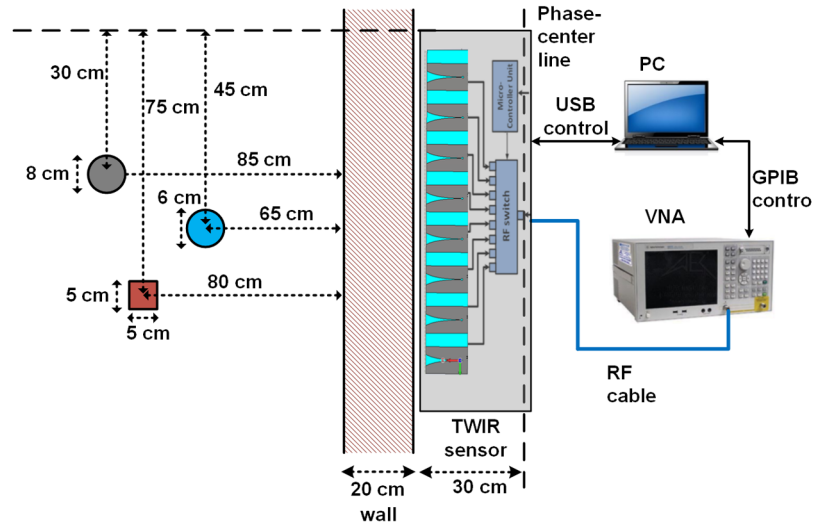


**Fig. 8** (a) Geometry for the stationary target experiment, (b) a picture for the pipes as targets, and (c) a scene from the experiment.

where the location and the dimensions of the metal pipes can be read. One pipe, made of iron, has a square cross section while the other two pipes, made of aluminum, have circular cross sections. The pipes were at different ranges and cross-range locations behind the wall as illustrated in Fig. 8(a). The wall has a thickness of  $\sim 20$  cm and is constructed by bricks. The surfaces of the bricks were covered with a concrete coating that had a thickness of  $\sim 3$  cm on both sides. In Fig. 8(b), a picture of the pipes that were used during the experiments is shown. A scene from the performed experiment can be seen in Fig. 8(c). During the experiment, the frequency of the VNA was altered from 3 to 8.5 GHz for a total of 201 distinct, linear frequency points.  $S_{11}$  measurements from the scene were collected with our automated data collection system for a total cross-range width of 88 cm. A background subtraction routine was employed to filter the reflections from the wall and the cross talk between the antenna elements. Then two-dimensional (2-D) range profile versus synthetic aperture image of the scene was obtained after inverse Fourier transforming the background-subtracted data along the frequency axis as plotted in Fig. 9(a). The range resolution of the images can be approximated as  $\delta r = c/(2 \cdot BW_f) = 30/(2 \cdot 5.5) = 2.73$  cm, where  $c$  is the speed of light and  $BW_f$  is the frequency bandwidth of the transmitted signal.

As expected, a hyperbolic type of image behavior was obtained due to the B-scan type of the data collection routine along the  $y$ -axis as shown in Fig. 9(a). This type of image feature is very

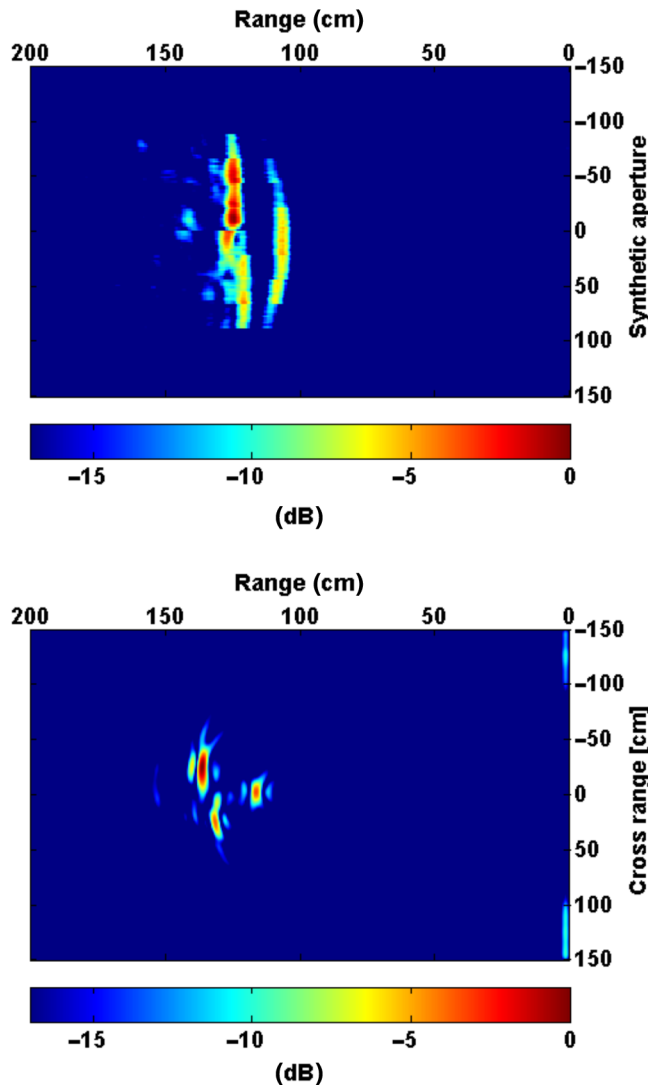


**Fig. 9** TWR image for (a) the range profile measurements and (b) the focused image after applying BPA.

common in ground penetrating radar imaging applications that have been well studied in the literature.<sup>26</sup> One powerful method to migrate the unfocused image behavior is to apply a back-projection algorithm (BPA) that can successfully focus the hyperbolic phenomena to its true location.<sup>27</sup> Before applying our BPA-based focusing algorithm, we have two reasonable assumptions: first, we assume that the delay caused by the wave propagation inside the wall can be neglected with respect to the total travel time of the EM wave. This approximation is practical because the wall thickness is 20 cm in our case, whereas the target is usually meters away from the wall. Second, the shift due to refraction of the EM wave in-and-out off the wall is assumed to be small when compared to the target's size. Taking the wall distance as 20 cm and the relative dielectric constant of the wall as 5,<sup>28</sup> the maximum azimuthal shift in the cross-range direction has been calculated to be around 4.88 cm for the maximum look-angle value of the main beam, i.e.,  $\pm 23.05$  deg. Therefore, this azimuthal shift value is negligible for our TWR operations when considering applications such as detecting moving humans.<sup>29</sup> As illustrated in Fig. 10, this shift in the image would not cause a significant error while locating any possible target behind the wall.

For the frequency domain operation of our TWR geometry given in Fig. 10, the details of our implementation for the BPA are explained by the following steps: first, we collect frequency diverse back-scattered electric field data  $E_s(k, y)$  in the cross-range axis  $y$ . Here,  $k = 2\pi f/v$  is the wavenumber, where  $f$  is the frequency and  $v$  is the speed of the EM wave inside or outside of the wall. Then, we apply one-dimensional (1-D) inverse Fourier transform (IFT) operation to the collected dataset as

$$E_s(r, y) = \text{IFT}[E_s(k, y)] = \int_{-\infty}^{\infty} E_s(k, y) \cdot \exp(j2kr) \cdot dk \quad (1)$$

to transform it onto a 2-D range-cross range plane. Next, we apply the projection-slice theorem<sup>30</sup> to relate  $E_s(r, y)$  to the measured data,  $S_\theta(k_r)$ . For the 2-D space, the projection-slice theorem states that the 1-D FT of the projection at the look-angle of  $\theta$  represents the slice of the 2-D FT projection of the geometry at the same angle, i.e.,

$$S_\theta(k_r) \equiv E_s(k_r, \theta). \quad (2)$$

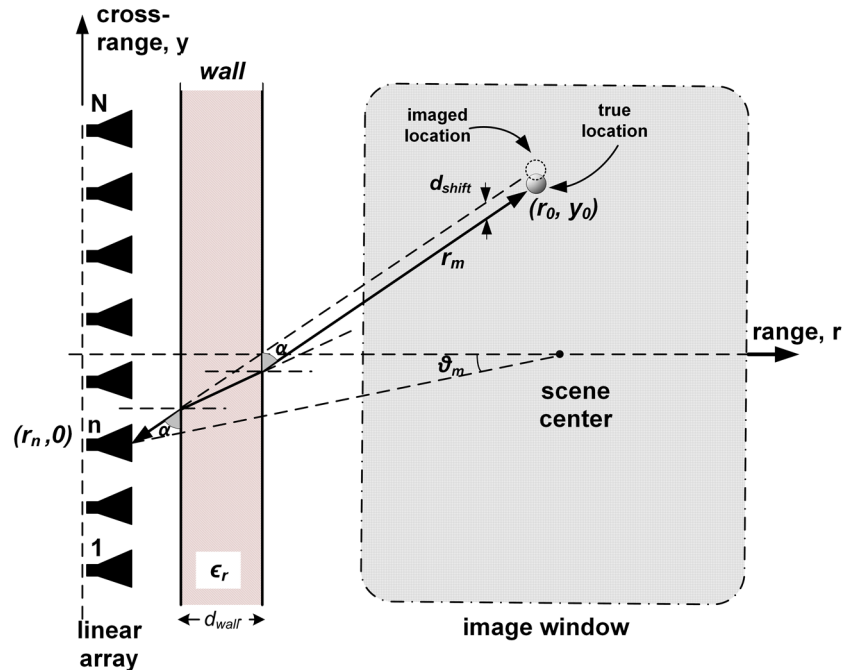


**Fig. 10** BPA focusing geometry for TWR imaging.

Therefore, the sampled representation of  $E_s(k_x, k_y)$  can be acquired from the FT of the projections  $S_\theta(k_r)$  measured at several observation angles. Using this principle, Eq. (1) can be reorganized as

$$E_s(r, y) = \int_{-\pi}^{\pi} \left[ \int_{-\infty}^{\infty} S_{\theta_m}(k_r) \cdot \exp(j2k_r r_m) k_r dk_r \right] \cdot d\theta_m. \quad (3)$$

The bracketed integral in Eq. (3) can be regarded as the 1-D IFT of the reflectivity function  $\Gamma(\theta_m) \triangleq S_{\theta_m}(k_r) \cdot k_r$  measured at  $r_m$ . If  $\rho_{\theta_m}(r_m)$  is the IFT of this function, Eq. (3) can be rewritten to be represented as

$$e(x, y) = \int_{-\pi}^{\pi} \rho_{\theta_m}(r_m) \cdot d\theta_m. \quad (4)$$

Equation (4) is the resultant migrated image in the spatial domain after applying the 2-D filtered BPA. For the geometry in Fig. 10, the implementation of the above-mentioned algorithm can be briefly summarized by the following steps:

- i. We preallocated an image matrix of zeros  $e(x, y)$  to record the values of the scene's reflectivity.
- ii. Then, we multiplied the collected spatial frequency data  $S_\theta(k_r)$  with  $k_r$ .
- iii. Next, we took the 1-D IFT of (2) to get  $\rho_{\theta_m}(r_m)$  which represented the filtered version of the range profile  $s_{\theta_m}(r)$ .

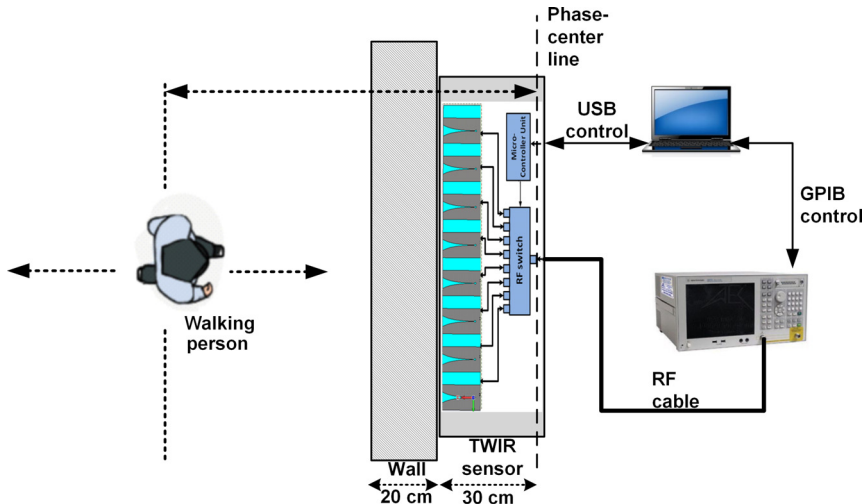


**Fig. 11** (a) Geometry for the moving target experiment and (b) a scene from the experiment.

- iv. For each image pixel for the selected image-window, we calculated the corresponding range value  $r_m$  and obtained its  $\rho_{\theta_m}(r_m)$  value through the nearest-neighbor interpolation scheme that is readily available in MATLAB.
- v. We added interpolated values to  $e(x, y)$ .
- vi. We repeatedly applied steps (ii) through (v) for all the observation angles  $\theta_m$  that corresponded to the TWR sensors with respect to the target in the scene.

We have employed the above-explained BPA to the unfocused image in Fig. 9(a) to get a focused one as plotted in Fig. 9(b). As seen from this figure, the image is very well focused as the pipes are pointed out at their true locations. The range and cross-range resolutions have been obtained by measuring at the  $-3$  dB widths of the hot spots in the radar image. Thanks to the linear array configuration of our TWR sensor, the cross-range ( $-3$  dB) resolution has been improved to be equal to be around  $10$  cm as measured from Fig. 9(b). The range resolution is measured to be around  $2.8$  cm which is very compatible with the theoretical value of  $2.73$  cm.

### 3.2 Experiment for a Moving Target

After successfully employing our TWR sensor for imaging stationary targets, we also tested its performance for the detection of targets in motion. For this purpose, the geometry in Fig. 11(a) was taken into consideration. During the experiment, the frequency of the VNA was altered from

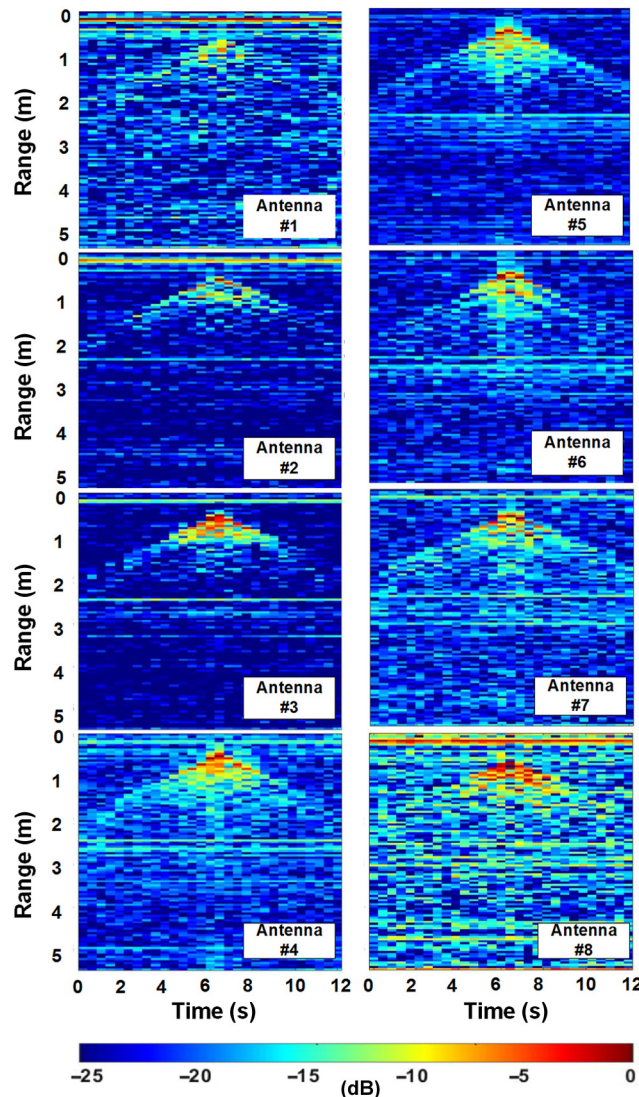


**Fig. 12** Range profiles with respect to time for each element of the linear array.

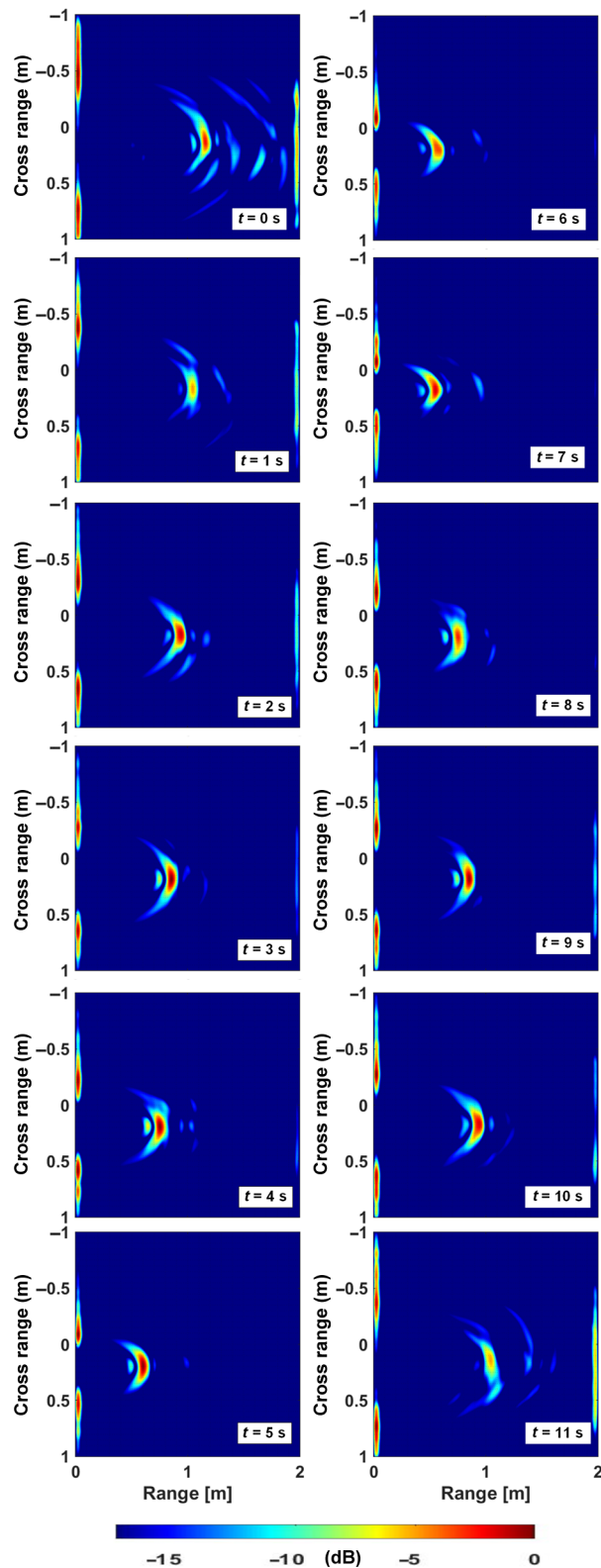


**Fig. 13** TWR images using back-projection focusing for human target moving (a) toward the radar and (b) away from the radar.

3 to 8.5 GHz with 27.5 MHz discrete frequency steps such that a total of 110 frequency samples were obtained.

During the experiment, the human target walked toward the wall and then away from the wall as pictured in Fig. 11(b). We have taken consecutive time snapshots of the scene as the target walks behind the wall. The sampling time of the snapshots was 1.05 s and was mainly dictated by the sampling period of the VNA. To image the change between the stationary TWR images, differential image matrices  $\Delta[\text{TWRI}(i, j)]_{k-1}$  were constructed by subtracting the  $k$ 'th image from the  $(k - 1)$ th image using the following equation:

$$\Delta[\text{TWRI}(i, j)]_{k-1} = [\text{TWRI}(i, j)]_k - [\text{TWRI}(i, j)]_{k-1}, \quad (5)$$

where  $[\text{TWIR}(i, j)]_k$  and  $[\text{TWIR}(i, j)]_{k-1}$  are the 2-D range-synthetic aperture image matrices for the  $k$ th and the  $(k - 1)$ th time-measurements, respectively. The raw range-profile images that were collected by eight-antenna elements are given in Fig. 12. A background subtraction routine was employed to lessen the reflections from clutter and other surrounding objects. Images show the range profiles (y-axis) with respect to time (x-axis). The changes in the range direction can be seen as the human target moves toward the radar and away from the radar in the images in Fig. 12. For these raw images, no signal processing routine was employed. For the first 13 distinct time snapshots, the human target walked toward the wall such that he started walking at a distance of 130 cm to the final destination of 85 cm from the phase center of our radar. After applying the methodology described above, a total of six differential images were obtained as plotted in Fig. 13(a), where the movement of the human target has been successfully imaged at his correct placement on the 2-D range, cross-range plane. One can also notice that the scattering from any stationary objects such as the wall was filtered out due to our image differencing routine and only the alterations between the successive images were detected. The cross talk between the antennas was also filtered out due to the employed change detection routine. For the last seven consecutive snap-shots, the human target walked away from the wall such that he started walking at a distance of 85 cm to the final destination of 130 cm from the phase center of our radar. Afterward, by applying the same imaging/focusing procedure as explained above, a total of six differential images were gathered as shown in Fig. 13(b). As easily observed from this figure, the movement of the target away from the wall is apparent and his true spatial positions are successfully located. There are two important observations that are worth mentioning about the constructed images: first, the radar images do not depict the actual size or shape of the target. As the target moves 9 cm while collecting the back-scattered data from the first channel and the last channel, what is imaged is the summed-up energy of the change between the first channel's distance and the last channel's distance as the SAR process was employed. Therefore, the constructed image relies on a region that is between these two points. Second, the target was not perceived by the sidelobes of the antennas within the array; therefore, no artifacts are apparent in the images.

The widths of the hot spots in Fig. 13 were examined by measuring the  $-3$ -dB widths of these image spots in the range and cross-range directions. It was found out that the  $-3$  dB image widths varies from 6 cm (for the nearest target) to 8.5 cm (for the farthest target) in the range direction, whereas  $-3$  dB image widths values were measured as 16 cm for the nearest walking target at 87 cm away from the radar and 44 cm for the farthest walking target at 130 cm from the radar. When considering the size of a human body for the walking man, these values of reflected energy change between the images are evaluated to be reasonable and provide a successful operation of differential TWR.

## 4 Conclusion

In this work, we have designed and manufactured a sensor that can be used to detect and image objects/targets behind a wall. The sensor consists of a linear array of UWB Vivaldi antennas, an RF switch, a microcontroller, and a power supply. First, elements of the array have been designed and optimized for the needs of TWR applications. The designed eight-element Vivaldi antenna array has been further optimized for the minimal mutual coupling and better radiation pattern features. Then the final design has been set and assembled to be used in TWR experiments.

The performance of the prototyped TWR sensor has been tested both for stationary and moving targets. For the stationary targets experiment, test objects were successfully imaged at their correct locations. While constructing the final TWR images, a back-projection type focusing algorithm has been utilized to better resolve images in the cross-range dimension. The image obtained by our TWR sensor has shown that the cross-range resolution has been improved thanks to multiple sampling of the backscattered data in this direction. In the second experiment, the TWR sensor has been assessed for the change detection imaging. For this purpose, a human target has walked toward and away from the wall while taking consecutive scene snapshots of backscattered field measurements. We applied an image differencing routine for the images that we have obtained with the help of our TWR sensor. Resultant differential images have validated that our sensor can successfully detect-and-image target movements behind the wall with good fidelity.

As a summary, this work contributes to the TWR technology in the sense that a radar sensor that can be practically used has been introduced and prototyped. Another contribution is the design of the light-weight, UWB antenna element that can also be readily used in TWR applications. This antenna provides the entire bandwidth from 3.5 to 8 GHz with suitable antenna radiation pattern characteristics for the detection of TWR targets behind the wall. The system design given in this paper can be further improved by adding more sensors in the cross-range axis and also utilizing a 2-D linear array in both cross-range dimensions. Although this sensor has been used together with a frequency-domain RF transceiver, it can also be operated if it is connected to a time-domain system for a much faster operation. Of course, the cross-range resolution can be further improved if more antennas are added to the array configuration at the price of a larger size and increased weight. For future work, as an improvement, we are planning a modified design with a quasimonostatic or a multistatic configuration so that we can get  $S_{21}$  measurements that will help boost the dynamic range of the TWR sensor.

## Acknowledgments

This work was supported by Mersin University Scientific Research Unit under Project No. BAP-FBE EEM(BY) 2011-7DR. Authors are thankful to Mustafa Berkam Biçer for his help for the production of antenna elements and programming the microcontroller unit.

## References

1. D. D. Ferris, Jr. and N. C. Currie, "A survey of current technologies for through-the-wall surveillance," *Proc. SPIE* **3577**, 62–72 (1999).
2. A. R. Hunt, "A wideband imaging radar for through-the-wall surveillance," *Proc. SPIE* **5403**, 590–596 (2004).
3. S. E. Borek, "An overview of through the wall surveillance for homeland security," in *IEEE Proc. of the 34th Applied Imagery and Pattern Recognition Workshop*, pp. 6–11 (2005).
4. H. D. Griffiths and C. J. Baker, "Radar imaging for combatting terrorism, imaging for detection and identification," in *Imaging for Detection and Identification*, pp. 29–48, Springer, Dordrecht, Netherlands (2007).
5. E. J. Baranoski, "Through-wall imaging: historical perspective and future directions," *J. Franklin Inst.* **345**(6), 556–569 (2008).
6. Y. Yang, Y. Wang, and A. E. Fathy, "Design of compact Vivaldi antenna arrays for UWB see through wall applications," *Prog. Electromagn. Res.* **82**, 401–418 (2008).
7. Y. J. Ren et al., "Compact ultrawideband UHF array antenna for through-wall radar applications," *IEEE Antennas Wirel. Propag. Lett.* **8**, 1302–1305 (2009).
8. F. Zhu et al., "Low-profile directional ultra-wideband antenna for see-through-wall imaging applications," *Prog. Electromagn. Res.* **121**, 121–139 (2011).
9. C. Ozdemir, *Inverse Synthetic Aperture Radar Imaging with MATLAB Algorithms*, John Wiley & Sons, Hoboken, New Jersey (2012).
10. Y. Mori et al., "Development of multi-path linear array radar at 10-20GHz," in *8th Int. Workshop on Advanced Ground Penetrating Radar (IWAGPR '15)*, Florence (2015).

11. G. Cui, L. Kong, and J. Yang, "A back-projection algorithm to stepped-frequency synthetic aperture through-the-wall radar imaging," in *Process of 1st Asian and Pacific Conf. on Synthetic Aperture Radar*, pp. 123–126 (2007).
12. F. Ahmad, M. Amin, and S. Kassam, "Synthetic aperture beamformer for imaging through a dielectric wall," *IEEE Trans. Aerosp. Electron. Syst.* **41**, 271–283 (2005).
13. Y. Jia, L. Kong, and X. Yang, "A novel approach to target localization through unknown walls for through-the-wall radar imaging," *Prog. Electromagn. Res.* **119**, 107–132 (2011).
14. <http://www.camero-tech.com/> (21 September 2016).
15. <http://www.retwis.com/en/retwis> (21 September 2016).
16. [http://www.ainfoinc.com/en/p\\_mwrf\\_sw.asp](http://www.ainfoinc.com/en/p_mwrf_sw.asp) (21 September 2016).
17. <https://www.arduino.cc/en/Main/arduinoBoardMega2560> (21 September 2016).
18. <http://www.mathworks.com/products/matlab/> (21 September 2016).
19. K. Guney and A. Akdagli, "Null steering of linear antenna arrays using a modified tabu search algorithm," *Prog. Electromagn. Res.* **33**, 167–182 (2001).
20. A. Akdagli and K. Guney, "Shaped-beam pattern synthesis of equally and unequally spaced linear antenna arrays using a modified tabu search algorithm," *Microwave Opt. Technol. Lett.* **36**, 16–20 (2003).
21. P. J. Gibson, "The Vivaldi aerial," in *Proc. 9th European Microwave Conf.*, pp. 101–105 (1979).
22. Y. Yang, Y. Wang, and A. E. Fathy, "Design of compact Vivaldi antenna arrays for UWB see through wall applications," *Prog. Electromagn. Res.* **82**, 401–418 (2008).
23. <https://www.cst.com/Products/CSTMWS> (21 September 2016).
24. <http://www.lpkf.com/products/rapid-pcb-prototyping/circuit-board-plotter/protomat-e33.htm> (21 September 2016).
25. [http://www.src-cables.com/catalog/SRC\\_SteelFlex\\_p6.pdf](http://www.src-cables.com/catalog/SRC_SteelFlex_p6.pdf) (21 September 2016).
26. C. Ozdemir et al., "A review on migration methods in B-scan ground penetrating radar imaging," *Math. Probl. Eng.* **2014**, 280738 (2014).
27. A. F. Yegulalp, "Fast backprojection algorithm for synthetic aperture radar," in *The Record of the 1999 IEEE Radar Conf.*, pp. 60–65 (1999).
28. V. Schejbal et al., "UWB propagation through walls," *Radioengineering* **15**(1), 17–24 (2006).
29. P. H. Chen and R. M. Narayanan, "Shifted pixel method for through-wall radar imaging," *IEEE Trans. Antennas Propag.* **60**(8), 3706–3716 (2012).
30. S. Vitebskiy et al., "Ultrawide-band, short pulse ground-penetrating radar: simulation and measurement," *IEEE Trans. Geosci. Remote Sens.* **35**, 762–772 (1997).

**Betül Yılmaz** received her BS and MS degrees in electrical and electronics engineering from Erciyes University and Mersin University in 2005 and 2008, respectively. She is an academic expert at Mersin University, Mersin, Turkey. She is pursuing her PhD in electrical and electronics engineering at Mersin University. Her current research interests include through-wall radar, ground-penetrating radar, and antenna design.

**Caner Özdemir** received his MSE and PhD degrees in electrical and computer engineering from the University of Texas, Austin in 1995 and 1998, respectively. From 1992 to 1993, he worked at the electronic warfare programs directorate of ASELSAN Electronic Industries Inc., Ankara, Turkey. From 1998 to 2000, he was a research scientist at ASTG Group of AlliedSignal Inc., Columbia, Maryland, USA. He is currently a professor at the Department of Electrical-Electronics Engineering, Mersin, Turkey.